

Temporal Scalability of Dynamic Volume Data using Mesh Compensated Wavelet Lifting

Wolfgang Schnurrer, Niklas Pallast, Thomas Richter, and André Kaup, *Fellow, IEEE*

Abstract—Due to their high resolution, dynamic medical 2D+t and 3D+t volumes from computed tomography (CT) and magnetic resonance tomography (MR) reach a size which makes them very unhandy for teleradiologic applications. A scalable representation offers the advantage of a down-scaled version which can be used for orientation or previewing, while the remaining information for reconstructing the full resolution is transmitted on demand. The wavelet transform offers the desired scalability but a very high quality of the lowpass band is crucial in order to use it as a down-scaled representant.

We propose an approach based on compensated wavelet lifting for obtaining a scalable representation of dynamic CT and MR volumes with very high quality. The mesh compensation is feasible to model the displacement in dynamic volumes which is mainly given by expansion and contraction of tissue over time. To achieve this, we propose an optimized estimation of the mesh compensation parameters to optimally fit for dynamic volumes. Within the lifting structure, the inversion of the motion compensation is crucial in the update step. We aim to take this inversion directly into account during the estimation step and can improve the quality of the lowpass sub-band by 0.63 dB and 0.43 dB on average for our tested dynamic CT and MR volumes at the cost of a increase of the rate by 2.4% and 1.2% on average.

Index Terms—Scalability, Discrete Wavelet Transforms, Motion Compensation, Computed Tomography, Magnetic Resonance Tomography, Signal Analysis

I. INTRODUCTION

A scalable representation of huge volume data offers the advantage of providing a down-scaled version much faster. This down-scaled representation can be utilized for faster browsing or orientation within the volume. Particularly when the volumes have to be transmitted, e.g., when the acquisition is done at a different location than the diagnosis or the volume data needs to be accessed by doctors, e.g., at rural areas. In the medical environment, lossless reconstruction is a crucial condition, although lossy compression has already been analyzed [1].

A wavelet-based approach as shown in Fig. 1 can provide a scalable representation as well as the necessary perfect reconstruction. In teleradiology, this enables new scenarios where a down-scaled representation can be transmitted faster. If only a specific part with a higher resolution is needed, solely the corresponding additional information has to be transmitted. By combining a high quality scalable representation with anatomic information [2] the specific part can be provided

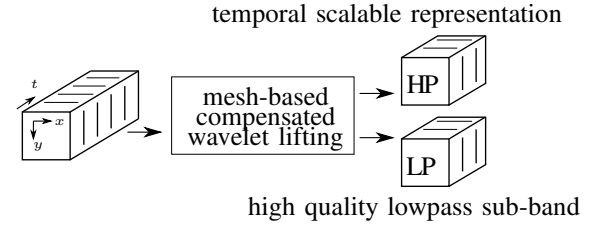


Figure 1. The block diagram shows the considered scenario. Compensated wavelet lifting is utilized to obtain a temporal scalable representation of a dynamic volume. Mesh-based methods are feasible to compensate the displacement in dynamic medical volumes and thus increase the quality of the lowpass sub-band to serve as down-scaled version.

lossless while the remaining part of the volume is available in a coarser representation. This volume of interest coding can be obtained by optimized coefficient coding [3]. Dependent on the application, it is additionally possible to reconstruct the original volume completely [4].

A wavelet-based approach offers a fundamentally different temporal scalability compared to a hybrid coding approach like H.265/HEVC [5], the current state of the art for coding video data. Using the hybrid approach, temporal scalability can be obtained by choosing an appropriate prediction scheme [6] supporting the skip of, e.g., every other frame. This corresponds to a sub-sampling without prior lowpass filtering. In contrast to that the lowpass sub-band from a wavelet transform results from sub-sampling after lowpass filtering. In medical applications, this comes with the advantage that structures, only visible within one original frame, do not disappear in the scalable representation due to sub-sampling. Displacements within the original volume that cannot be modeled by the compensation method are still contained within the lowpass sub-band.

In the medical environment, the Digital Imaging and Communications in Medicine (DICOM) standard [7] is used for communication. This standard contains several coding methods for image data. In practice, usually a frame by frame coding using lossless JPEG [8] is used for coding.

The lowpass sub-band of a wavelet transform is computed as weighted average. By design, displacement in the signal can cause a blurry lowpass sub-band with ghosting artifacts. This drawback can be addressed by incorporating feasible compensation methods directly into the transform. In video coding, a compensated wavelet transform in temporal direction is called Motion Compensated Temporal Filtering (MCTF) [9]. Video sequences mostly contain translatory motion. Consequently, block-based methods are mainly used for compen-

The authors are with the Chair of Multimedia Communications and Signal Processing, Friedrich-Alexander-University Erlangen-Nürnberg (FAU), Cauerstr. 7, 91058 Erlangen, Germany (e-mail: wolfgang.schnurrer@fau.de; niklas.pallast@fau.de; thomas.richter@fau.de; andre.kaup@fau.de).

sation [9], [10]. However, the motion model of translatory movement of objects does not fit well for dynamic medical volumes [11]. Within wavelet lifting of video sequences, mesh-based compensation has also proven its better suitability [12]. The displacement over time is mainly given by expansion and contraction of tissue. Mesh-based compensation methods have shown their ability to model the deforming displacement well [13], [14]. Mesh-based methods have also shown to be well suited to model the deformation within dynamic medical volumes in other applications, e.g., for image registration [15].

The inversion of the mesh-based compensation is, however, most often not needed and thus not considered when estimating the parameters of the mesh deformation. However, within the update step of wavelet-lifting, the compensation has to be inverted [16]. This inversion is not only necessary but very important in order to move the remaining high frequent information to the corresponding position for the lowpass frame. Consequently, it is also very important for the quality of the lowpass sub-band. So far in the current literature, only the compensation is considered during the estimation of the parameters for the mesh-based compensation.

The characteristic of the dynamic medical volumes and their containing displacement can be used directly for providing properties of the mesh. The deforming displacement to be compensated results from expansion and contraction of tissue over time. The displacement can be described as smooth without discontinuities, i.e., there are no discontinuities in the mesh either. A regularizer can be used to prefer similar movement of neighboring grid points and thus a smooth motion vector field [17]. The regularizer also prevents small local movements in the mesh due to noise. Medical images usually cover the complete displacement, so the border grid points of the mesh can only move along the border but remain there.

In this article, we propose an approach to obtain a scalable representation of dynamic volumes based on mesh compensated wavelet lifting. The approach is based on our work previously published: In [18], a compensated wavelet transform in z -direction is analyzed. In [13], we compared triangular and quadrilateral meshes where quadrilateral meshes show a better performance for a compensated wavelet transform in temporal direction of dynamic CT volumes. In [14], 3-D mesh compensation is examined.

In this article, we introduce a novel criterion for the mesh-based motion estimation and a new method to evaluate the smoothness of the mesh deformation. The article is outlined as follows. Section II starts with a brief review of compensated wavelet lifting and introduces mesh-based compensation in II-B. The estimation for the mesh deformation follows in section III with our proposed adaptations and our proposed metric. Simulation results are presented in section IV. Section V gives the conclusions.

II. MESH COMPENSATED WAVELET LIFTING

The lifting structure is an efficient way to compute a wavelet transform. Therefore, wavelet filters are factorized into the lifting structure [19]. The lifting structure consists of two steps.

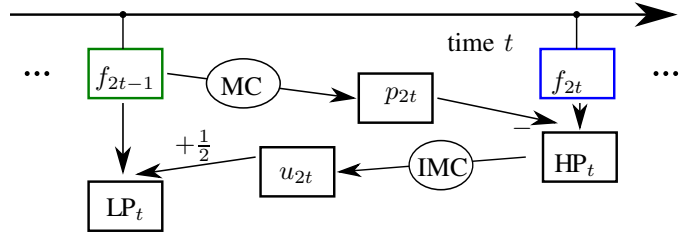


Figure 2. Lifting structure for the Haar wavelet transform with compensation (MC). The sequence f is decomposed into a highpass sub-band and a lowpass sub-band. In the update step of the lifting structure, the compensation has to be inverted (IMC).

In the prediction step, the highpass sub-band is computed according to

$$HP_t = f_{2t} - f_{2t-1} \quad (1)$$

where f_t denotes a frame at time step t of the signal to be transformed.

In the update step, the lowpass sub-band LP_t is computed according to

$$LP_t = f_{2t-1} + \left[\frac{1}{2} HP_t \right] \quad (2)$$

utilizing the already computed highpass sub-band coefficients HP_t in (1).

In (2), the relationship between highpass sub-band and lowpass sub-band becomes immediately visible. In addition to that, the lifting structure offers several more advantages. An integer transform can be obtained very easily by introducing rounding operators [4] around the fractional parts as in (2). Thereby, rounding errors are avoided. The perfect reconstruction property makes this transform feasible and very interesting for medical applications as it does not only offer a scalable representation but also the possibility to reconstruct the original signal without loss. Furthermore, arbitrary compensation methods can be implemented directly into the transform [20] without losing the perfect reconstruction property. Blurriness and artifacts within the lowpass sub-band caused by displacement over time can be avoided by utilizing a feasible compensation method.

A. Compensated Wavelet Lifting

For obtaining temporal scalability, the wavelet transform is applied in temporal direction. The highpass coefficients HP_t of a compensated wavelet transform are computed in the prediction step according to

$$HP_t = f_{2t} - \lfloor \mathcal{W}_{2t-1 \rightarrow 2t}(f_{2t-1}) \rfloor. \quad (3)$$

Instead of the original frame f_{2t-1} , a predictor is subtracted from f_{2t} , denoted by the warping operator $\mathcal{W}_{2t-1 \rightarrow 2t}$ [20]. The compensation is called MC in Fig. 2. The result of the warping operator $\mathcal{W}_{2t-1 \rightarrow 2t}$ is a predictor p_{2t} for the current frame f_{2t} based on the reference frame f_{2t-1} and can be written as

$$\begin{aligned} p_{2t}(x_c, y_c) &= \mathcal{W}_{2t-1 \rightarrow 2t}(f_{2t-1}) \\ &= \tilde{f}_{2t-1}(x_r(x_c, y_c), y_r(x_c, y_c)) \end{aligned} \quad (4)$$

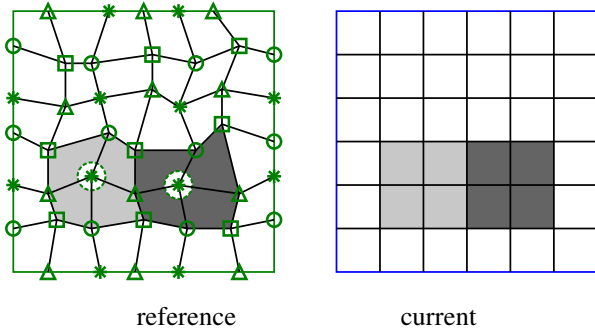


Figure 3. The green deformed mesh on the left corresponds to the reference frame f_{2t-1} and the blue mesh to the current frame f_{2t} . The prediction p_{2t} is computed by applying the bilinear transform for each quadrilateral i in f_{2t-1} according to its deformation. The update u_{2t} is obtained by applying the inverse bilinear transform for every quadrilateral in f_{2t} respectively.

where $x_r(x_c, y_c)$ and $y_r(x_c, y_c)$ contain the mapping for pixels within the current frame to the pixels in the reference frame. For a given position in the current frame, $x_r(x_c, y_c)$ and $y_r(x_c, y_c)$ provide the corresponding position in the reference frame. The tilde denotes to the necessary interpolation to obtain intensity values at non-integer positions.

In the update step of the compensated wavelet transform, the lowpass coefficients $LP_{\text{Haar},t}$ are computed by

$$LP_t = f_{2t-1} + \left[\frac{1}{2} \mathcal{W}_{2t \rightarrow 2t-1} (HP_t) \right]. \quad (5)$$

The index of \mathcal{W} in (5) shows the inverse compensation in the update step. This is crucial to achieve an equivalent wavelet transform [16]. The inversion of the compensation warps the remaining high frequency structures within HP_t to their corresponding positions within f_{2t-1} to provide a reasonable update. The inversion is denoted by IMC in Fig. 2. For a compensated wavelet transform, the mesh-based compensation method has the advantage that it is invertible [12], [17].

B. Mesh-based Compensation

In this Section, the mesh-based compensation and its inversion is explained in assumption of the mesh parameters, i.e., the motion vectors of the grid points, to be known. The estimation of the grid point motion follows in Section III. In general, a mesh-based compensation is computed according to the deformation of a mesh. Therefore, one mesh is laid over the reference frame and one is laid over the current frame, see Fig. 3. The mesh of the reference frame is deformed as shown in Fig. 3 on the left. The predictor for the current compensation is computed by warping each deformed quadrilateral in the reference frame to its corresponding quadrilateral in the current frame, exemplarily shown for the gray quadrilaterals. The connectivity of the mesh represents the image transform used. A triangular mesh leads to an affine transform [21] while a quadrilateral mesh leads to a bilinear transform [22]. The smoother motion vector field of a quadrilateral mesh showed to be more feasible for the compensation of the deformation within dynamic medical volumes [13].

Several properties for the mesh-based compensation can be derived from the assumptions for the displacement over time.

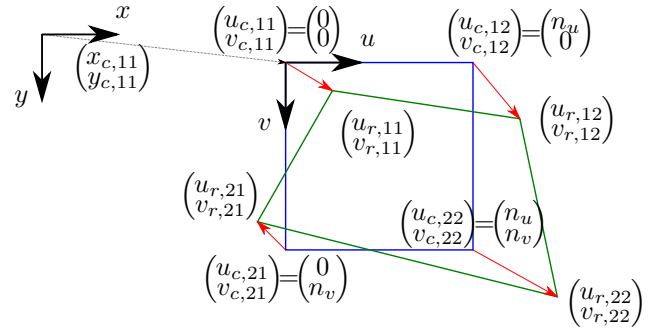


Figure 4. Diagram of the bilinear transform for a quadrilateral showing the local coordinate system. The local coordinate system has its origin in the upper left of the blue quadrilateral, i.e., within the current frame. The coordinates of the quadrilateral within the current frame are labeled by (u_c, v_c) while the coordinates of the green deformed quadrilateral within the reference frame are labeled by (u_r, v_r) . The red arrows show the motion vectors of the grid points and thus describe the deformation of the mesh.

The displacement results from expansion and contraction of tissue over time. This deformation corresponds to a smooth displacement without motion discontinuities. There will be no change in the mesh topology like breaking apart at a motion boundary. Displacement occurs only within a frame, so the outer shape of the mesh remains on the frame border. This means the four grid points at the frame corner remain fixed. Grid points on the left and right border may move up and down only while grid points on the upper and lower border may move left and right only. Thereby unconnected pixels [9] do not occur.

The mesh-based compensation is a feasible approach and can also be interpreted as a sub-sampling of a dense smooth motion vector field. The grid points represent the sampling points and the motion vectors in between are obtained by bilinear interpolation.

For each quadrilateral, the deformation is given by the image transform that corresponds to the grid point movement. Considering the i -th quadrilateral, the coordinates in the reference frame (x_r, y_r) can be computed from the coordinates in the current frame (x_c, y_c) by applying the bilinear transform. Therefore, a local coordinate system (u, v) is introduced [23]. Its' origin is in the upper left grid point of the quadrilateral in the current frame, as shown in Fig. 4. The (u, v) coordinates are computed by subtracting the upper left corner $(x_{c,11}, y_{c,11})$ from the coordinates in the (x, y) system. The bilinear transform is then computed according to (6) and (7).

$$\begin{aligned} u_r(u_c, v_c) &= a_{11,i}u_c v_c + a_{12,i}u_c + a_{13,i}v_c + a_{14,i} \quad (6) \\ v_r(u_c, v_c) &= a_{21,i}u_c v_c + a_{22,i}u_c + a_{23,i}v_c + a_{24,i} \quad (7) \end{aligned}$$

For simplicity, index i is omitted in the following. The calculations have to be repeated for every quadrilateral. The coefficients a_{11} to a_{24} of the bilinear image transform matrix are computed from the motion of the grid points of the current quadrilateral.

$$n_u = x_{c,12} - x_{c,11} \quad n_v = y_{c,21} - y_{c,11}$$

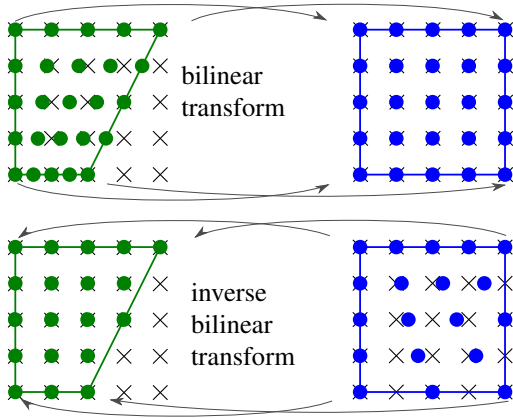


Figure 5. Mesh-based compensation and its inversion in detail showing the source and the destination of the pixel coordinates. In the upper part, the compensation is shown according to the bilinear transform of the quadrilateral. In the lower part, the inverse compensation is shown according to the inverse bilinear transform of the quadrilateral. Crosses mark positions of the regular pixel grid where intensity values are available, respectively necessary. For points beside the regular pixel grid, the corresponding intensities have to be computed by interpolation.

$$\begin{aligned}
 a_{11} &= u_{r,22} - u_{r,12} + u_{r,11} - u_{r,21} \\
 a_{21} &= v_{r,22} - v_{r,12} + v_{r,11} - v_{r,21} \\
 a_{12} &= \frac{u_{r,12} - u_{r,11}}{n_u} & a_{22} &= \frac{v_{r,12} - v_{r,11}}{n_v} \\
 a_{13} &= \frac{u_{r,21} - u_{r,11}}{n_u} & a_{23} &= \frac{v_{r,21} - v_{r,11}}{n_v} \\
 a_{14} &= \frac{u_{r,11}}{n_u} & a_{24} &= \frac{v_{r,11}}{n_v}
 \end{aligned}$$

The coordinates in the (x, y) system can then be computed by moving the origin back, i.e. by adding the upper left corner $(x_{c,11}, y_{c,11})$ to the (u, v) coordinates. For the coordinates of the grid points, the correspondence simplifies to (8) and (9), where $mv_x(x_c, y_c)$ contains the x component of the motion vector of the grid points and $mv_y(x_c, y_c)$ the respective y component.

$$x_r = mv_x(x_c, y_c) + x_c \quad (8)$$

$$y_r = mv_y(x_c, y_c) + y_c \quad (9)$$

The deformation of every quadrilateral is given by the corresponding bilinear transform. A detailed example is illustrated in the upper part of Fig. 5. The bilinear transform of the green quadrilateral on the left to the blue quadrilateral on the right is shown. Intensity values at a regular pixel grid are marked by black crosses. To obtain intensity values for the blue points on the right, corresponding values are needed from the green positions on the left. The green positions are computed by the bilinear transform. They are obtained by interpolation from the available values at the regular pixel grid.

C. Inversion of the Bilinear Transform

Within the update step of the lifting structure (2), the compensation has to be inverted [16]. During the estimation

process, movements of the grid points are only allowed if the corresponding bilinear transform remains invertible. This will be shown in Section (III-B). For an invertible bilinear transform, the inverse can be computed [23] by solving (6) and (7) for (u_c, v_c) . For example, solving (6) for u_c results in

$$u_r - a_{13}v_c - a_{14} = (a_{11}v_c + a_{12})u_c. \quad (10)$$

Inserting (10) into (7) and solving for v_c results in a quadratic equation (11).

$$\alpha v_c^2 + \beta v_c + \gamma = 0 \quad (11)$$

$$\alpha = a_{23}a_{11} - a_{21}a_{13}$$

$$\beta = a_{21}u_r - a_{11}v_r + a_{24}a_{11}$$

$$-a_{21}a_{14} - a_{22}a_{13} + a_{23}a_{12}$$

$$\gamma = a_{22}u_r - a_{12}v_r + a_{24}a_{12} - a_{22}a_{14}$$

$$v_{c1,2} = \frac{-\beta \pm \sqrt{\beta^2 - 4\alpha\gamma}}{2\alpha}, \text{ where } \alpha \neq 0 \quad (12)$$

The desired solution for v_c can then be determined by choosing the one that lies within the quadrilateral in the current frame. For $\alpha = 0$, (11) simplifies to $\beta v_c + \gamma = 0$.

The inverse of the compensation for the update step is obtained by computing this mapping for all pixels in all quadrilaterals. Due to the mapping, pixel values are needed at fractional pixel positions within the highpass sub-band HP_t . This is illustrated in the lower part of Fig. 5. The blue positions on the right are computed from the green positions by the inverse bilinear transform. The desired intensity values at the blue points on the right are computed by interpolation from the available positions at the regular pixel grid.

In [12], an approximation of the inversion is done by negating the motion vectors. The approximation error increases, the smaller the quadrilaterals and the larger the motion of the grid points are [13]. This can lead to an increase of the energy in the highpass sub-band and artifacts in the lowpass sub-band [13].

III. PROPOSED GRID POINT MOTION ESTIMATION

The most challenging part is the estimation of the grid point motion. Neighboring grid points influence each other. In order to find the optimum solution, all combinations of motion have to be tested. This is computationally by far too complex. In [21], [22], an efficient iterative refinement method is proposed. Independent grid points of the mesh are organized into sets. In every refinement iteration, the sets are processed subsequently but all grid points within one set can be processed in parallel. This is illustrated in Fig. 3 on the left. Grid points from one set are marked with the same symbol and can be processed in parallel. The two grid points within the gray marked quadrilaterals can be optimized without interfering with each other.

The following subsections explain the different steps of the iterative refinement of the grid point motion estimation; namely our adaptations to the used hierarchic estimation [17], the restriction of the movement, the proposed regularization, and finally the proposed metric for finding the optimum update

within one refinement step. Finally a novel metric is introduced to evaluate the smoothness of the resulting mesh deformation.

A. Hierarchic Estimation

With the aim to estimate the movement of larger structures better, a hierarchic estimation approach can be used [17]. The deformation of the mesh is estimated with different quadrilateral sizes, i.e., from coarse to fine mesh resolution. From left to right in Fig. 6, the quadrilateral size is reduced. The first mesh has a quadrilateral size of s_1 . After a few iterations, the quadrilateral size is reduced to s_2 by adding the blue colored grid points. The motion vectors of the blue grid points are obtained by bilinear interpolation from the neighboring green grid points. Subsequently, the motion vectors of all grid points are refined. Afterwards, the same principle is applied for the red grid points. With every hierarchy step, more grid points are added and the quadrilateral size is reduced. Thus, the mesh is able to compensate finer displacements with every hierarchy step.

In [17], a mesh-based prediction is computed. The estimation can be accelerated by using a larger refinement step size d_{sr} for the larger mesh size to obtain a faster estimation [17]. The compensation has to be inverted in the update step of the lifting structure. To avoid converging to a minimum further away in periodic texture structures, we the step size is kept small and constant.

Only the number of grid points is increased during the estimation. The estimation is performed on the full frame resolution. An additional reduction of the resolution of the frame during the estimation leads to worse results, especially when fine detailed structures are omitted due to downsampling. For this reason, the frame resolution was not reduced during the estimation process.

Another advantage of a hierarchic approach is that movements of structures that lie within different smaller quadrilaterals can be covered with a deductive approach by starting with very large quadrilaterals. Only a few iterations are computed for a small refinement search range to avoid finding a 'wrong' local minimum for periodic structures.

B. Restrict Movement of the Grid Points

There are several reasons for preferring or allowing only certain updates during the refinement. First of all, the motion compensation has to be inverted in the update step of the wavelet transform. Movements of the grid points are only allowed when the resulting image transform remains invertible.

For explaining the procedure, the refinement of the center grid point P , shown in Fig. 7, is considered in the following.

The determinant of the Jacobian of a bilinear transform (6), (7) can be evaluated as sufficient criterion for invertibility [24], [25]. The determinant of the Jacobian (13) is dependent on the image coordinates and forms a plane in 3-D space. The necessary derivatives can be computed according to (14). The bilinear transform is invertible, when the determinant is positive for every position in a quadrilateral [24]. To fulfill this, it is sufficient to evaluate the planar equation of the

determinant at the four corner points of a quadrilateral. For stability reasons, we further add a threshold $\Delta > 0$.

$$\begin{aligned} \det \begin{pmatrix} \frac{\partial u_r}{\partial u_c} & \frac{\partial u_r}{\partial v_c} \\ \frac{\partial v_r}{\partial u_c} & \frac{\partial v_r}{\partial v_c} \end{pmatrix} &= \frac{\partial u_r}{\partial u_c} \frac{\partial v_r}{\partial v_c} - \frac{\partial v_r}{\partial u_c} \frac{\partial u_r}{\partial v_c} \quad (13) \\ &= (a_{21}a_{11} - a_{21}a_{11}) u_c v_c \\ &\quad + (a_{12}a_{21} - a_{22}a_{11}) u_c \\ &\quad + (a_{23}a_{11} - a_{13}a_{21}) v_c \\ &\quad + (a_{12}a_{23} - a_{13}a_{22}) \\ &\geq \Delta \end{aligned}$$

$$\begin{aligned} \frac{\partial u_r(u_c, v_c)}{\partial u_c} &= a_{11}v_c + a_{12} & \frac{\partial u_r(u_c, v_c)}{\partial v_c} &= a_{11}u_c + a_{13} \\ \frac{\partial v_r(u_c, v_c)}{\partial u_c} &= a_{21}v_c + a_{22} & \frac{\partial v_r(u_c, v_c)}{\partial v_c} &= a_{21}u_c + a_{23} \end{aligned} \quad (14)$$

The black arrows in the center of Fig. 7 illustrate the refinement positions for the motion vector of grid point P in the current iteration. For every tested position in the refinement procedure, for each neighboring quadrilateral of P , namely $ABPD$, $BCEP$, $DPGH$, and $PEHG$, the entries of the bilinear transform matrix (6), (7) have to be computed. Then, for each neighboring quadrilateral, the determinant of the Jacobian can be evaluated. To maintain the property for the inversion, a candidate for the refinement is refused if one of the determinants is smaller than threshold Δ .

C. Proposed Regularizer for Preferring a Smooth Motion Vector Field

For preferring a smoother mesh deformation, a regularizer can be used during the estimation procedure [17]. The more similar motion vectors of neighboring grid points are, the smoother the resulting mesh deformation will be. Thereby, the cost function for finding the optimum candidate in a refinement step is extended by a regularizer term r (15). This regularizer term decreases, the more similar the current motion vector candidate $(mv_{x,cand}, mv_{y,cand})$ is to the motion vectors of the neighboring grid points, i.e., the smaller the variance of the motion vectors [17]. In addition to the literature [17], we propose to incorporate the current quadrilateral size s of the hierarchic estimation procedure into the regularizer. The smaller the quadrilateral size s , the larger the influence of the regularizer r to the cost function. By utilizing a regularizer, local minima in the estimation are avoided by increasing the cost for locally very fine-grained deviations of the mesh.

$$\begin{aligned} r(mv_{x,cand}, mv_{y,cand}) &= \quad (15) \\ &= \frac{1}{s} \frac{1}{8} \sum_{(x_{GP}, y_{GP}) \in \text{NGP}} \left((mv_x(x_{GP}, y_{GP}) - mv_{x,cand})^2 + \right. \\ &\quad \left. + (mv_y(x_{GP}, y_{GP}) - mv_{y,cand})^2 \right)^{\frac{1}{2}} \end{aligned}$$

An example is given in Fig. 7. The regularizer is computed for every valid candidate, illustrated by black arrows

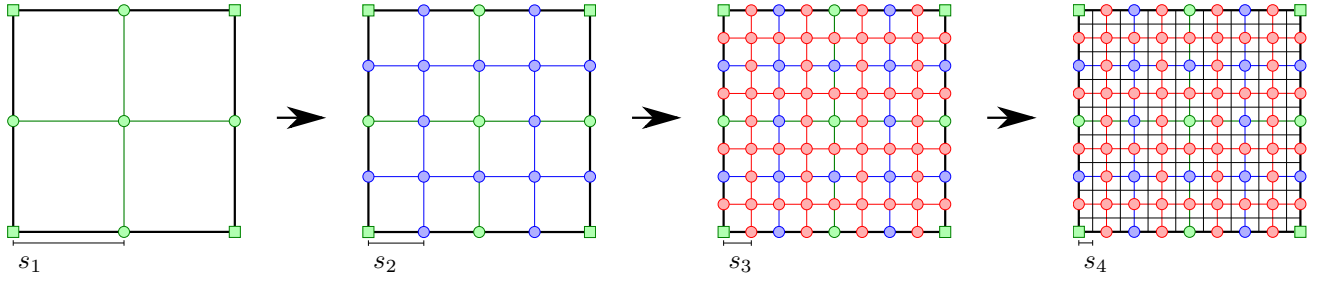


Figure 6. The illustration shows a mesh which corresponds to the complete frame at different steps of the hierarchic estimation. The symbols mark the grid points of the mesh. By the very coarse mesh grid in the beginning on the left, the mesh can better represent larger moving areas. In every hierarchic step, grid points are added and the mesh can adapt to smaller local displacements as well.

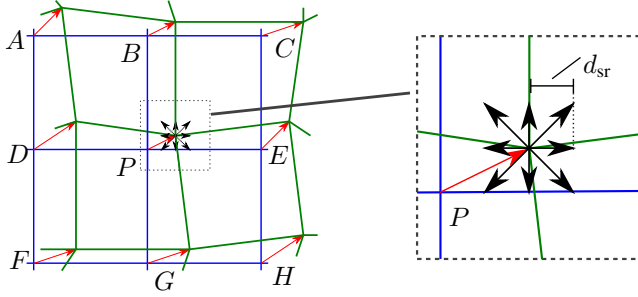


Figure 7. Refinement for grid point P is considered. The black arrows point to the candidates that are tested for the refinement of the movement of P with search range d_{sr} . On the right, a zoom for the marked region on the left is shown.

at the tip of the motion vector of grid point P . The motion vectors of the eight neighboring grid points $NGP = \{A, B, C, D, E, F, G, H\}$ of the currently considered grid point P show a smooth movement in the upper right direction. The cost for a candidate pointing to the lower right will be higher compared to a candidate pointing in direction of the neighbors. For a candidate pointing to a different direction than the neighbors, the similarity metric of the corresponding deformed quadrilateral has to be small enough to justify this movement. The next section combines the regularizer with similarity terms and introduces our proposed cost function for the refinement procedure.

D. Proposed Metric for Estimation

To determine an optimum candidate in the refinement procedure, a cost function is utilized. So far [17], the cost function only consists of a similarity term evaluating the prediction error and a regularizer. The origin of the similarity term is illustrated in Fig. 8 on the right. The bilinear transform results in a prediction for the blue colored quadrilateral on the right. For the blue points, the mean squared error MSE_{comp} is computed and used for the similarity term.

So far, the state of the art metric J_{soa} is used where λ controls the influence of the regularizer r .

$$J_{soa} = MSE_{comp} + \lambda r \quad (16)$$

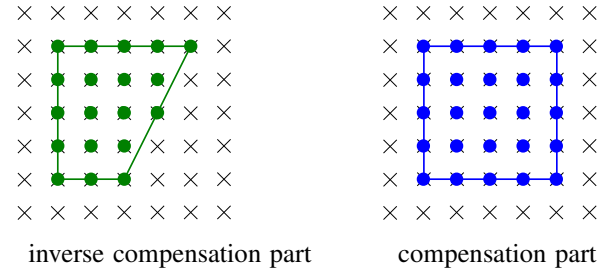


Figure 8. For choosing the optimum candidate during the estimation process, the proposed metric evaluates the similarity by two parts. For the compensation part, the deformed quadrilateral of the reference frame is mapped to current frame by applying the bilinear transform as shown in the upper part of Fig. 5 and the MSE is computed. The pixels contributing to MSE_{comp} are marked on the right. For the inverse compensation part, the quadrilateral is mapped from the current frame to the reference frame as shown in the lower part of Fig. 5 and the MSE is computed again. The pixels contributing to $MSE_{invcomp}$ are marked on the right.

The inverse compensation is not considered so far, i.e., how well the inverse transform of the blue quadrilateral matches the green quadrilateral. This is illustrated by the green points on the left of Fig. 8. To incorporate the quality of the inversion into the metric, the mean squared error $MSE_{invcomp}$ for the green points on the left is computed.

The proposed metric (17) is computed by

$$J_{prop} = MSE_{comp} + MSE_{invcomp} + \lambda r. \quad (17)$$

The normalization of the sum of squared differences to the number of elements is necessary to address the different number of elements for the compensation and inverse compensation part, shown by the different number of blue and green points in Fig. 8. To address this, the mean squared error is used. With this metric, the optimum candidate is determined during the iterative refinement procedure.

E. Proposed Smoothness Evaluation of the Mesh Deformation

In order to determine the smoothness of the mesh with one value, a metric was developed. The smoothness of the deformation is represented by $S \in (0; 1]$, where values closer to 1 correspond to a shape more similar to a square.

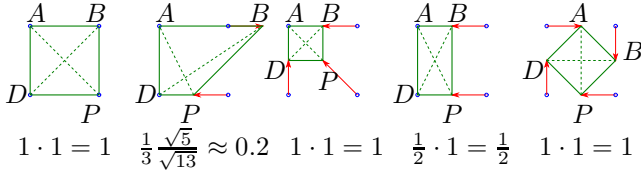


Figure 9. Examples for the proposed evaluation of the mesh smoothness and the corresponding values of S_{ABPD} .

Table I
DYNAMIC MEDICAL VOLUMES USED FOR SIMULATION

	CT		MR							
x	512	192	192	192	156	192	192	156	156	156
y	512	256	256	256	192	156	156	192	192	192
z	128	1	1	1	1	1	1	1	1	1
t	10	60	60	60	24	24	24	10	10	10

For the green deformed quadrilateral $ABPD$ shown in Fig. 7, S_{ABPD} is computed according to

$$S_{ABPD} = \frac{\min(\overline{AB}, \overline{BP}, \overline{PD}, \overline{DA})}{\max(\overline{AB}, \overline{BP}, \overline{PD}, \overline{DA})} \cdot \frac{\min(\overline{AP}, \overline{BD})}{\max(\overline{AP}, \overline{BD})}. \quad (18)$$

The first fraction evaluates the ratio between the minimum and the maximum length of the edges. The second fraction evaluates the respective ratio for the diagonals of the quadrilateral. Fig. 9 shows examples for the smoothness value of different deformations. The smoothness value becomes smaller with increasing fine-granular local mesh deformation. Therefore, a value closer to 1 is desired. This value is computed for all quadrilaterals of the mesh. To obtain one meaningful value for the smoothness of the complete mesh, the smoothness value S of the complete mesh is computed by averaging the results from all quadrilaterals. On average, a value closer to 1 corresponds to a smoother deformation of the complete mesh. This metric is used to evaluate the smoothness of the mesh deformation after the iterative refinement procedure.

IV. SIMULATION RESULTS

For the simulation, we used dynamic volumes from computed tomography (CT¹) and magnetic resonance tomography (MR²) showing sequences of the beating heart. Tab. I lists details for the spatial and temporal resolution. The intensity values have a co-domain of 12 bit. The spatial resolution of the CT volumes is typically higher. To be independent of the actual co-domain, a scaling to $[0; 1]$ is done for the estimation process of the mesh deformation. To evaluate our proposed metric, we perform one compensated wavelet decomposition step in temporal direction. For the 3-D+t CT volume, we took the 10 time steps at every position in z -direction as sequence. This results in 128 CT sequences.

Fig. 10 shows two successive frames of the CT volume at slice position $z = 51$. A detail of the lowpass sub-band

¹The CT volume data set was kindly provided by Siemens Healthcare.

²The MR volume data sets were kindly provided by doctor Jacques Beckmann, radiologist at Katharinen Hospital, Unna.

Table II
DETAILS FOR THE HIERARCHIC STEPS USED IN THE SIMULATION.

		hierarchic estimation						subpixel extension	
CT	s	256	128	64	32	16	8	8	8
	d_{sr}	1	1	1	1	1	1	0.5	0.25
	#iter	3	3	4	5	6	9	1	1
	sum		6	10	15	21	30	31	32
MR	s			64	32	16	8	8	8
	d_{sr}			1	1	1	1	0.5	0.25
	#iter			10	5	6	9	1	1
	sum				15	21	30	31	32

of the Haar transform without compensation is shown on the right. Due to the large displacement from f_1 to f_2 , the lowpass sub-band gets blurred and most details are lost. The separated structures in the original frames are mixed up and cannot be distinguished anymore. This example visualizes the need for feasible compensation methods.

For the mesh-based compensation, the threshold for the determinant of the Jacobian is set to $\Delta = 0.2$. Thereby, the invertibility of the compensation is maintained. Geometrically, this means, the quadrilaterals remain convex and do not diverge, e.g., to triangles [25]. Tab. II lists the parameters used for the iterative hierarchic estimation procedure for the CT and the MR volumes. Intensity values at non-integer positions are calculated by bilinear interpolation. For the CT volumes, the hierarchic estimation starts with 3 iterations using a search range $d_{sr} = 1$ at a quadrilateral size of $s = 256$. In the next hierarchic step 3 iterations are computed at $s = 128$, etc. After the second hierarchic step, 6 iterations are computed. The row 'sum' counts the total number of iterations. For the resolutions of the MR volumes, a maximum quadrilateral size of $s = 64$ is reasonable to start the hierarchic estimation with a large grid size where the quadrilaterals have about the same size and s is a power of 2. The last two columns of Tab. II correspond to the extension where the influence of a subpixel search range d_{sr} was tested.

For the example given in Fig. 10, Fig. 11 shows details of the lowpass sub-band from a compensated Haar transform using different parameters for the mesh. The regularizer parameter was set to $\lambda = 0.0004$. On the left, no hierarchic estimation was used, i.e. 30 iterations with $d_{sr} = 1$ were computed at grid size $s = 8$. In the last two columns, hierarchic estimation according to Tab. II was applied. In the first two columns, the state of the art metric J_{soa} and in the last column our proposed metric J_{prop} was used during the estimation process. The given PSNR values show the similarity of the lowpass sub-band frames to the original frames. Usually, only the similarity between the lowpass sub-band frame and the corresponding original frame is considered by evaluating $\text{PSNR}(f_1, LP_1)$. However, the lowpass sub-band is a representation for the complete original volume. To evaluate additionally the similarity to the current frame, $\text{PSNR}(f_2, \mathcal{W}_{1 \rightarrow 2}(LP_1))$ is evaluated. Therefore, the lowpass sub-band frame LP_1 is warped to the time step of the current frame $\mathcal{W}_{1 \rightarrow 2}$.

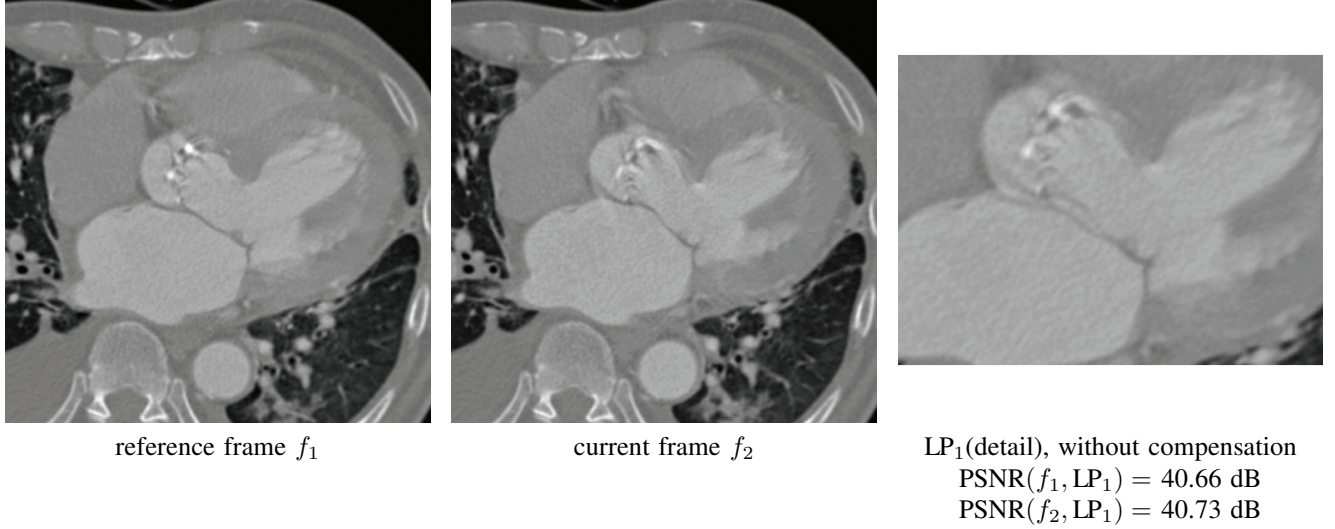


Figure 10. Visual example for two successive original frames at slice $z = 51$ of the CT volume. From left to right, the reference frame f_1 , the current frame f_2 , and a detail of the corresponding frame LP_1 of the lowpass sub-band using a Haar transform without compensation is shown.

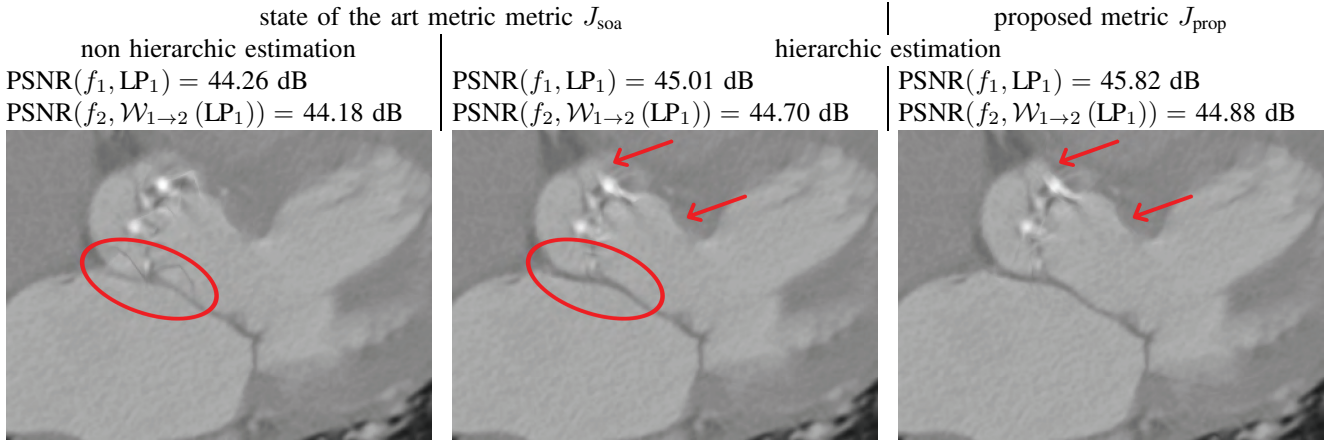


Figure 11. Visual comparison of the resulting lowpass sub-bands from a mesh compensated wavelet transform. The regularizer parameter was set to $\lambda = 0.0004$. On the left, the state of the art metric J_{soa} without hierarchic estimation was used. In the center, the result is shown using the state of the art metric and hierarchic estimation. On the right, the result of our proposed metric J_{prop} with hierarchic estimation is shown. For the proposed metric, the corresponding mesh is shown on the bottom of in Fig. 12. From left to right, the artifacts marked in red disappear.

Table III
 PSNR IN DB, MESH SMOOTHNESS S , AND RATE FOR THE MESH PARAMETERS FOR DIFFERENT VALUES OF THE PARAMETER λ FOR THE REGULARIZER

		state of the art metrik J_{soa}					proposed metrik J_{prop}				
		$\lambda = 0$	0.0003	0.0004	0.0005	0.0007	$\lambda = 0$	0.0003	0.0004	0.0005	0.0007
CT	PSNR (f_{2t-1}, LP_t)	49.28	48.04	47.85	47.70	47.44	49.70	48.66	48.48	48.33	48.09
	PSNR ($f_{2t}, \mathcal{W}_{2t-1 \rightarrow 2t}(LP_t)$)	48.56	47.45	47.28	47.13	46.90	48.38	47.73	47.60	47.49	47.31
	smoothness S	0.393	0.856	0.878	0.893	0.913	0.397	0.791	0.820	0.839	0.866
	filesize in kbyte	5.35	2.12	1.98	1.88	1.76	5.33	2.55	2.36	2.23	2.05
MR	PSNR (f_{2t-1}, LP_t)	49.98	48.86	48.70	48.56	48.36	50.02	49.26	49.13	49.00	48.82
	PSNR ($f_{2t}, \mathcal{W}_{2t-1 \rightarrow 2t}(LP_t)$)	48.31	48.28	48.22	48.17	48.12	48.23	48.36	48.32	48.28	48.23
	smoothness S	0.693	0.913	0.921	0.927	0.934	0.697	0.885	0.897	0.906	0.916
	filesize in kbyte	0.48	0.27	0.26	0.25	0.24	0.48	0.30	0.29	0.28	0.26

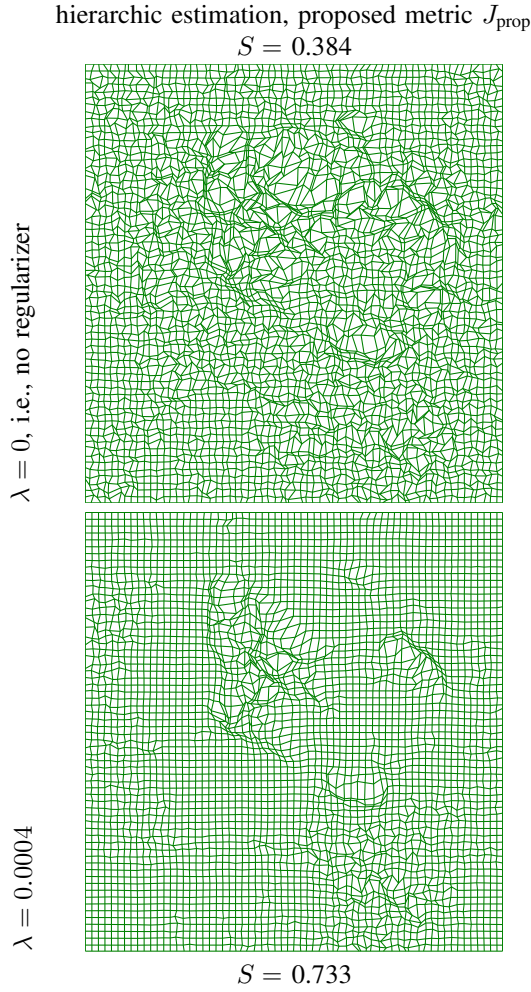


Figure 12. Comparison of the influence of the regularizer on the resulting mesh. Our proposed metric J_{soa} and hierarchic estimation was used. The upper mesh results from the estimation without regularization. For the lower mesh, the regularizer parameter was set so $\lambda = 0.0004$ and a detail of the corresponding frame of the lowpass sub-band is shown in Fig. 11 on the right.

Without the hierarchic estimation, visual artifacts are clearly visible in left image of Fig. 11. The sequence contains displacements which are too large to be considered by the small quadrilaterals of the non hierarchic approach. The convergence of the mesh to local minima results in disturbing artifacts in the lowpass sub-band showing structures which have not been in the original volume. By starting the estimation with very large quadrilaterals, larger and global displacements can be modeled better. By using the hierarchic estimation, the artifacts marked by the red ellipse mostly disappear in the center image of Fig. 11. However, some artifacts and blurriness remain in the center image visible in the area pointed by the red arrows. Especially the light gray structure is sharper in the right image. Although the bilinear transform is inverted, artifacts can occur when only one direction of the image transform is considered. The detail shown on the right results from our proposed metric and contains sharper structures. Compared to the state of the art metric used in the center, the visual quality is improved significantly.

Fig. 12 shows the impact of the regularizer. The upper

mesh results from the estimation without regularization. Fine granular local deviations of the quadrilaterals are visible. Due to noise in the original volume, the mesh is deformed even in mostly flat areas without displacement. By incorporating a feasible regularizer, the resulting deformation of the mesh is smoother and corresponds more to the assumptions for the displacement within dynamic volumes. Solely the combination of regularizer and hierarchic estimation yield to a reasonable estimation. The lower mesh in Fig. 12 corresponds to the detail shown on the right of Fig. 11.

The results for the CT and the MR volumes are very similar, hence the average for all volumes is given in Tab. III. The table shows that by incorporating a regularizer ($\lambda > 0$), the PSNR results become a little smaller. Basically, the regularizer modifies the cost function in the estimation process. Deformations which might be optimum with respect to the squared error are made more expensive in case of causing a non smooth mesh deformation. The strength of the regularizer can be controlled using the parameter λ . For $\lambda = 0$, the regularizer has no influence on the determination of the grid point movement. For $\lambda > 0$, the restriction on the grid point movement increases with an increasing value of λ . Deviations due to noise in smooth regions can be avoided by using a reasonable value of λ . If the value is chosen to high, the mesh cannot compensate the displacement anymore.

From left to right, Tab. III lists the results obtained with mesh-based compensation using the state of the art metric J_{soa} and our proposed metric J_{prop} with increasing λ . As can be seen from the results in Tab. III, turning off the regularizer ($\lambda = 0$) leads to a significant decrease in the mesh smoothness and a significant increase in the rate needed for the mesh parameters. The rate is obtained using [26]. J_{soa} only optimizes the compensation direction. The decrease of the similarity of the lowpass sub-band frames to the current frames PSNR (f_{2t-1}, LP_{2t}) for $\lambda = 0$ results from the consideration of the inversion by our proposed metric J_{prop} . For the influence of the regularizer r , a value of $\lambda = 0.0004$ yields a reasonable trade-off between fine-granular mesh deformation, i.e., local adaption with respect to the assumptions on the displacement over time and smoothness S of the mesh.

As shown by the example in Fig. 11 on the right, the visual quality is increased significantly by our proposed metric. There are different reasons for the improvement. First, by taking the inversion of the compensation into account, another similarity term is added to the optimization function (17). Thereby, the relative influence of the regularizer is decreased. The impact can be seen by the decrease of the mesh smoothness on the right half of Tab. III. However, this is not the only reason. Without regularization, our proposed metric is able to increase the PSNR (f_{2t-1}, LP_{2t}) from 49.28 dB to 49.70 dB. for the CT volumes. The mesh smoothness also increases slightly. The inversion of the compensation is also taken into account by J_{prop} . Among others, the effect of the bilinear interpolation is considered which is necessary to obtain intensity values on the regular pixel as presented in Section II-B. With our proposed metric J_{prop} , the quality of the lowpass sub-band can be improved significantly. Furthermore, the similarity to the original reference frame as well as the current frame can

Table IV
AVERAGE FILE SIZE PER FRAME IN KBYTE

		f_t			no comp			mesh comp, $J_{\text{soa}}, \lambda = 0.0004$				mesh comp, $J_{\text{prop}}, \lambda = 0.0004$			
		ref f_{2t-1}	cur f_{2t}	sum	HP	LP	sum	HP	LP	MV	sum	HP	LP	MV	sum
MR CT	JPEG 2000	147.36	147.36	294.72	142.06	140.96	283.02	142.00	144.06	1.98	288.04	142.67	144.80	2.36	289.83
	SPECK	155.56	155.56	311.12	149.52	149.58	299.09	148.98	152.19	1.98	303.15	149.40	152.75	2.36	304.51
	JPEG 2000	18.45	18.47	36.92	17.18	17.65	34.83	16.64	18.35	0.26	35.25	16.59	18.39	0.29	35.27
	SPECK	21.46	21.47	42.93	18.86	20.66	39.51	18.34	21.12	0.26	39.71	18.29	21.17	0.29	39.74

Table V
PSNR IN dB AND MESH SMOOTHNESS S FOR THE SUBPIXEL EXTENSIONS. FOR COMPARISON, THE FIRST COLUMN LISTS THE RESULTS FOR THE HIERARCHIC ESTIMATION. THE NEXT TWO COLUMNS LIST THE RESULTS FOR THE SUBPIXEL EXTENSION WITH REGULARIZER ENABLED. THE LAST TWO COLUMNS LIST THE RESULTS FOR DISABLING THE REGULARIZER FOR THE FINAL TWO ITERATIONS.

		proposed metric J_{prop}					
		hier. est.	$\lambda = 0.0004$		$\lambda = 0$		
		$d_{\text{sr}} 0.5$	$d_{\text{sr}} 0.5, 0.25$	$d_{\text{sr}} 0.5$	$d_{\text{sr}} 0.5, 0.25$		
CT	$\overline{\text{PSNR}(f_{2t-1}, \text{LP}_t)}$	48.48	48.60	48.66	48.94	49.12	
	$\overline{\text{PSNR}(f_{2t}, \mathcal{W}_{2t-1-2t}(\text{LP}_t))}$	47.60	47.70	47.75	47.95	48.10	
	S	0.820	0.822	0.828	0.711	0.665	
MRT	$\overline{\text{PSNR}(f_{2t-1}, \text{LP}_t)}$	49.13	49.39	49.55	50.20	50.66	
	$\overline{\text{PSNR}(f_{2t}, \mathcal{W}_{2t-1-2t}(\text{LP}_t))}$	48.32	48.48	48.55	48.12	48.13	
	S	0.897	0.898	0.903	0.818	0.799	

be improved. Using our proposed metric the average PSNR can be increased from by 47.85 dB to 48.48 dB by 0.63 dB for the CT volumes.

To evaluate the compressibility of the resulting sub-bands from the compensated wavelet transform in temporal direction, the sub-bands have been coded lossless using two standard state of the art wavelet coefficient coders, namely JPEG2000 [27] and SPECK [28]. Therefore, an additional 5 level dyadic decomposition in xy -direction of each frame was applied using the LeGall 5/3 wavelet. Tab. IV lists the resulting average file size per frame in kbyte for the highpass sub-band and the lowpass sub-band to see the contribution of the sub-bands to the overall file size. The rate is obtained using [26]. Overall, both methods perform in a very similar way. A wavelet decomposition in temporal direction leads to better results than coding a volume slice-by-slice. The best coding results can be obtained by applying a wavelet transform in temporal direction without compensation. However, uncompensated displacement causes artifacts in the lowpass sub-band as shown in Fig. 10. Lossless reconstruction is a crucial condition for medical image data. Due to the data acquisition process, noisy structures are very similar in neighboring frames. Usually a transform is applied along neighboring pixels. By incorporating a compensation method into the transform, it is applied on the motion trajectory [9]. This makes it difficult to exploit the similar noisy structures for coding [13], [14]. The results for the sub-bands from the compensated transform are in a similar range. For obtaining a high quality lowpass sub-band, the rate increases by about 2.4% compared to uncompensated

wavelet transform.

In coincidence with the subpixel estimation for block-based motion compensation [5], we tested two extensions using a subpixel d_{sr} in the refinement. Therefore, one iteration after the hierarchic estimation is computed using an $d_{\text{sr}} = \frac{1}{2}$ followed by an iteration using $d_{\text{sr}} = \frac{1}{4}$. In the first extension, the parameter for the regularizer was not changed. In the second extension the regularizer was deactivated for the final two iterations. The resulting meshes are shown in Fig. 13. In the first column, the first iteration with $d_{\text{sr}} = \frac{1}{2}$ was computed. In the last two columns, both iterations were computed. Only the subpixel refinement in the end is considered, therefore the maximum movement of a grid point equals a distance of 0.75 pixel. As a result, the meshes look very similar. Nevertheless, performing the subpixel refinement without regularizer, i.e., $\lambda = 0$, the resulting mesh on the right is not as smooth as the mesh in the center. Tab. V lists the results for all simulated volumes. For comparison, the first column repeats the results from the hierarchic estimation before the subpixel extensions. The subpixel extensions can further improve the similarity of the lowpass sub-band to the original sequence. The smoothness can slightly be improved if the regularizer is kept enabled. The metric for the smoothness confirms that disabling the regularizer for the last two iterations leads to very fine granular deviations in the mesh. This also increases the file size for lossless coding, listed in Tab. VI. With the regularizer, the file size for the CT volume is reduced slightly after the first iteration of the subpixel extensions.

Keeping the regularizer enabled for a subpixel refinement as final step of the iterative estimation process is advantageous for the mesh smoothness, the compressibility of the sub-bands and the quality of the lowpass sub-band.

V. SUMMARY AND CONCLUSION

A scalable representation of a dynamic volume entails several advantages. We propose a method to obtain a temporal scalable representation of dynamic volumes. By incorporating feasible compensation methods into the wavelet transform, the quality of the lowpass sub-band can be improved by 0.63 dB and 0.43 dB for CT and MR volumes at the cost of a small rate increase. A high quality of the lowpass sub-band of a compensated wavelet transform is necessary when it shall be utilized as down-scaled version of the signal.

In addition to the compensation in the prediction step, the inversion in the update step is also a crucial part of compensated wavelet lifting. Current research has not considered the inversion of the compensation during the estimation. We added this missing part to the model for finding the optimum

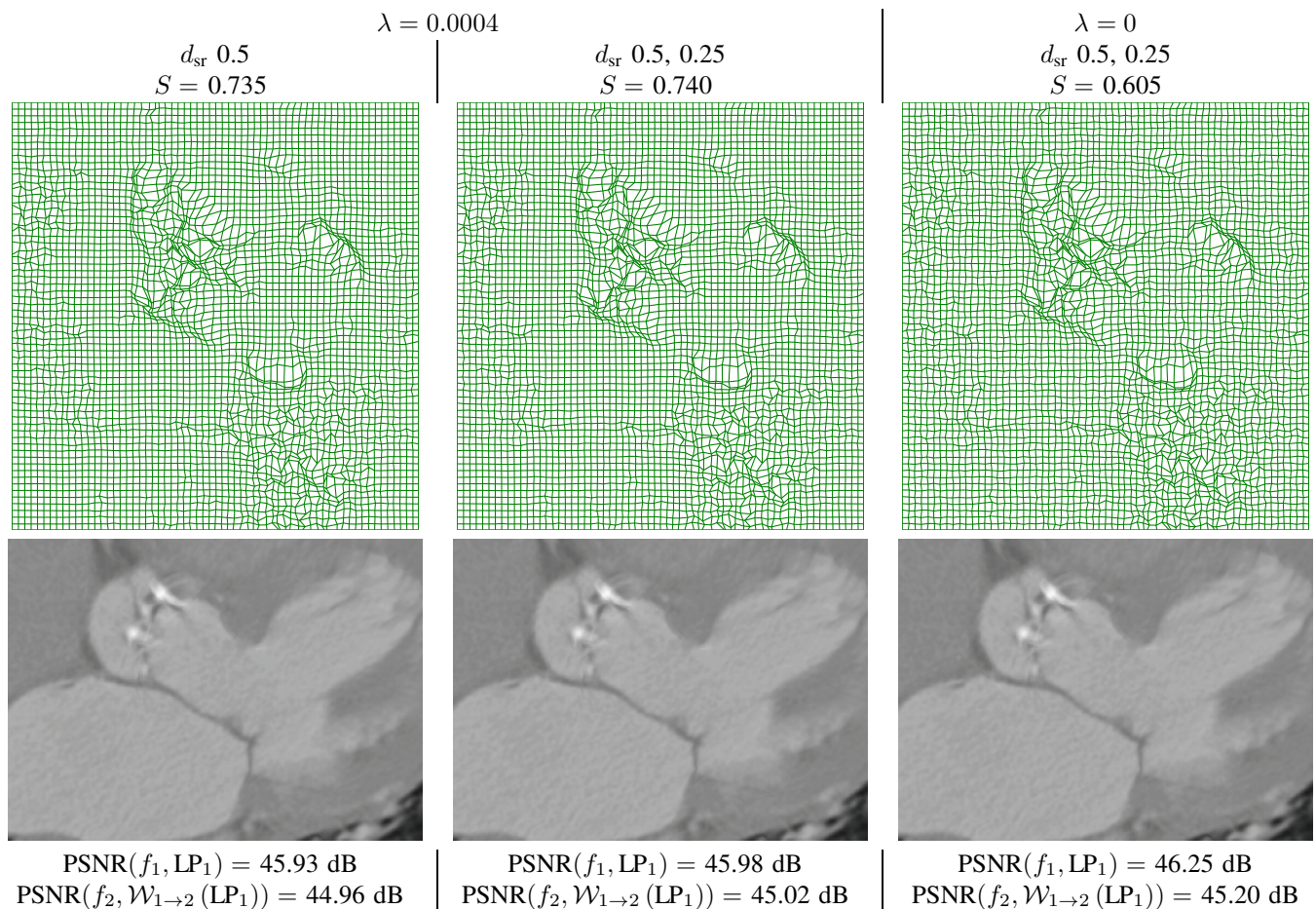


Figure 13. Visual comparison for computing LP_1 , $z = 51$ of the cardiac CT volume using the subpixel estimation in addition to the hierarchic estimation. The first row shows the deformed meshes resulting from the estimation using a subpixel search range in addition to the hierarchic estimation. The images in the second row show details from the corresponding lowpass sub-bands LP_1 . On the right, the regularizer has been disabled ($\lambda = 0$) for these final two refinement iterations. For all cases, the proposed metric J_{prop} has been used.

Table VI
AVERAGE FILE SIZE PER FRAME IN KBYTE FOR THE TWO SUBPIXEL EXTENSIONS

		$\lambda = 0.0004$								$\lambda = 0$							
		subpixel 0.5			sum	subpixel 0.5 0.25			sum	subpixel 0.5			sum	subpixel 0.5 0.25			sum
MR	CT	HP	LP	MV		HP	LP	MV		HP	LP	MV		HP	LP	MV	
MR	JPEG 2000	141.73	144.10	3.48	289.31	142.11	144.92	4.84	291.87	142.15	144.99	4.67	291.81	143.59	146.03	6.72	296.34
	SPECK	148.73	152.23	3.48	304.43	148.85	152.88	4.84	306.56	148.79	152.98	4.67	306.44	149.81	153.76	6.72	310.29
	JPEG 2000	16.58	18.29	0.46	35.33	16.49	18.29	0.58	35.36	16.48	18.45	0.58	35.51	16.45	18.42	0.77	35.64
	SPECK	18.28	21.14	0.46	39.88	18.18	21.21	0.58	39.96	18.17	21.30	0.58	40.04	18.12	21.33	0.77	40.22

parameters for the compensation method. The lowpass sub-band can be additionally improved by extending the metric, to serve as high quality scalable representation with smaller temporal resolution.

ACKNOWLEDGMENT

The authors gratefully acknowledge that this work has been supported by the Deutsche Forschungsgemeinschaft (DFG) under contract number KA 926/4-2.

REFERENCES

- [1] R. Loose, R. Braunschweig, E. Kotter, P. Mildner, R. Simmler, and M. Wucherer, "Kompression digitaler Bilddaten in der Radiologie - Ergebnisse einer Konsensuskonferenz," in *RöFo. Fortschritte auf dem Gebiet der Röntgenstrahlen und der bildgebenden Verfahren*, vol. 181, no. 07, 2008, pp. 32–37.
- [2] A. Cavallaro, F. Graf, H.-P. Kriegel, M. Schubert, and M. Thoma, "Region of Interest Queries in CT Scans," in *Advances in Spatial and Temporal Databases*. Springer, 2011, pp. 56–73.
- [3] V. Sanchez, R. Abugharbieh, and P. Nasiopoulos, "3-D Scalable Medical Image Compression With Optimized Volume of Interest Coding," *IEEE Transactions on Medical Imaging*, vol. 29, no. 10, pp. 1808–1820, Oct. 2010.
- [4] A. Calderbank, I. Daubechies, W. Sweldens, and B.-L. Yeo, "Lossless Image Compression Using Integer to Integer Wavelet Transforms," in *Proceedings IEEE International Conference on Image Processing (ICIP)*, Washington, DC, USA, Oct. 1997, pp. 596–599.
- [5] G. Sullivan, J. Ohm, W.-J. Han, T. Wiegand, and T. Wiegand, "Overview of the High Efficiency Video Coding (HEVC) Standard," *IEEE Transactions on Circuits and Systems for Video Technology*, vol. 22, no. 12,

- pp. 1649–1668, Dec. 2012.
- [6] G. Sullivan, J. Boyce, Y. Chen, J.-R. Ohm, C. Segall, and A. Vetro, “Standardized extensions of high efficiency video coding (hevc),” *IEEE Journal of Selected Topics in Signal Processing*, vol. 7, no. 6, pp. 1001–1016, Dec. 2013.
 - [7] O. Pianykh, *Digital Imaging and Communications in Medicine (DICOM)*. Springer, 2008.
 - [8] G. Wallace, “The JPEG Still Picture Compression Standard,” *IEEE Transactions on Consumer Electronics*, vol. 38, no. 1, pp. 18–34, Feb. 1992.
 - [9] J.-R. Ohm, “Three-Dimensional Subband Coding with Motion Compensation,” *IEEE Transactions on Image Processing*, vol. 3, no. 5, pp. 559–571, Sep. 1994.
 - [10] S. Choi and J. W. Woods, “Motion-Compensated 3-D Subband Coding of Video,” *IEEE Transactions on Image Processing*, vol. 8, no. 2, pp. 155–167, Feb. 1999.
 - [11] A. Nosratinia, N. Mohsenian, M. Orchard, and B. Liu, “Interframe Coding of Magnetic Resonance Images,” *IEEE Transactions on Medical Imaging*, vol. 15, no. 5, pp. 639–647, Oct. 1996.
 - [12] A. Secker and D. Taubman, “Lifting-Based Invertible Motion Adaptive Transform (LIMAT) Framework for Highly Scalable Video Compression,” *IEEE Transactions on Image Processing*, vol. 12, no. 12, pp. 1530–1542, Dec. 2003.
 - [13] W. Schnurrer, T. Richter, J. Seiler, and A. Kaup, “Analysis of Mesh-Based Motion Compensation in Wavelet Lifting of Dynamical 3-D+T CT Data,” in *Proceedings IEEE International Workshop on Multimedia Signal Processing (MMSP)*, Banff, Canada, Sep. 2012, pp. 152–157.
 - [14] W. Schnurrer, T. Richter, J. Seiler, C. Herglotz, and A. Kaup, “3-D Mesh Compensated Wavelet Lifting for 3-D+T Medical CT Data,” in *Proceedings IEEE International Conference on Image Processing (ICIP)*, Paris, France, Oct. 2014, pp. 3631–3635.
 - [15] D. Frakes, L. Dasi, K. Pekkan, H. Kitajima, K. Sundareswaran, A. Yoganathan, and M. Smith, “A New Method for Registration-Based Medical Image Interpolation,” *IEEE Transactions on Medical Imaging*, vol. 27, no. 3, pp. 370–377, Mar. 2008.
 - [16] N. Bozinovic, J. Konrad, W. Zhao, and C. Vazquez, “On the Importance of Motion Invertibility in MCTF/DWT Video Coding,” in *Proceedings IEEE International Conference on Acoustics, Speech, and Signal Processing (ICASSP)*, Philadelphia, PA, USA, Mar. 2005, pp. 49–52.
 - [17] G. Heising, D. Marpe, H. Cycon, and A. Petukhov, “Wavelet-Based Very Low Bit-Rate Video Coding Using Image Warping and Overlapped Block Motion Compensation,” *Proceedings IEE Vision, Image and Signal Processing*, vol. 148, no. 2, pp. 93–101, Apr. 2001.
 - [18] W. Schnurrer, J. Seiler, and A. Kaup, “Analysis of Displacement Compensation Methods for Wavelet Lifting of Medical 3-D Thorax CT Volume Data,” in *Proceedings IEEE Visual Communications and Image Processing (VCIP)*, San Diego, CA, USA, Nov. 2012, pp. 1–6.
 - [19] I. Daubechies and W. Sweldens, “Factoring Wavelet Transforms into Lifting Steps,” *Journal of Fourier Analysis and Applications*, vol. 4, no. 3, pp. 247–269, May 1998.
 - [20] J. Garbas, B. Pesquet-Popescu, and A. Kaup, “Methods and Tools for Wavelet-Based Scalable Multiview Video Coding,” *IEEE Transactions on Circuits and Systems for Video Technology*, vol. 21, no. 2, pp. 113–126, Feb. 2011.
 - [21] Y. Nakaya and H. Harashima, “Motion Compensation Based on Spatial Transformations,” *IEEE Transactions on Circuits and Systems for Video Technology*, vol. 4, no. 3, pp. 339–356, Jun. 1994.
 - [22] G. Sullivan and R. Baker, “Motion Compensation for Video Compression Using Control Grid Interpolation,” in *Proceedings IEEE International Conference on Acoustics, Speech, and Signal Processing (ICASSP)*, Toronto, Canada, Apr. 1991, pp. 2713–2716.
 - [23] G. Heising, K. Barthel, W. Johannsen, and C. Steinbach, “Blocking Artefact Free Video Coding based on a Bilinear Forward Image Warping Model,” in *Proceedings IEEE International Conference on Image Processing (ICIP)*, vol. 1, Oct. 1997, pp. 275–278.
 - [24] C. A. Glasbey and K. V. Mardia, “A Review of Image-warping Methods,” *Journal of applied statistics*, vol. 25, no. 2, pp. 155–171, 1998.
 - [25] Y. Wang and O. Lee, “Use of Two-dimensional Deformable Mesh Structures for Video Coding. Part I - The Synthesis Problem: Mesh-based Function Approximation and Mapping,” *IEEE Transactions on Circuits and Systems for Video Technology*, vol. 6, no. 6, pp. 636–646, Dec. 1996.
 - [26] J. Fowler, “QecPack: An Open-Source Software Library for Quantization, Compression, and Coding,” in *Proceedings Applications of Digital Image Processing XXIII*, vol. 4115, San Diego, CA, USA, Aug. 2000, pp. 294–301.
 - [27] C. Christopoulos, A. Skodras, and T. Ebrahimi, “The JPEG2000 Still Image Coding System: An Overview,” *IEEE Transactions on Consumer Electronics*, vol. 46, no. 4, pp. 1103–1127, Nov. 2000.
 - [28] W. A. Pearlman and A. Islam, “Embedded and Efficient Low-complexity Hierarchical Image Coder and Corresponding Methods Therefor,” US Patent US 6,671,413, Dec., 2003.